ACS APPLIED POLYMER MATERIALS

pubs.acs.org/acsapm Article

Controlling Fiber Morphologies Arising from Room-Temperature Cure Blowing

Aditya Banerji, Mahesh K. Mahanthappa, and Christopher J. Ellison*

Cite This: ACS Appl. Polym. Mater. 2023, 5, 7841−7853 Read Online

ACCESS | Metrics & More | Article Recommendations | Supporting Information

ABSTRACT: Cure blowing is a fiber manufacturing process whereby simultaneous extrusion and photopolymerization of a liquid monomer mixture produces nonwoven fibers of cross-linked polymers at room temperature with little or no solvent. Using a lab-scale die resembling that used in commercial melt blowing processes, we demonstrate the dependence of final cure blown fiber morphology on a competitive interplay of three categories of parameters corresponding to the photopolymerization kinetics, monomer mixture fluid properties, and process operating conditions, by quantifying and comparing the respective characteristic timescales for vitrification, fluid relaxation, and fiber flight. By constructing timescale-dependent morphology maps for two chemically distinct model systems, these timescales are found to account for the observed fiber morphology transitions irrespective of the photopolymerization mechanism. These morphology maps furnish a predictive tool for implementing different photopolymerization chemistries to achieve cure blown fibers with prescribed morphologies and properties for a wide array of applications.

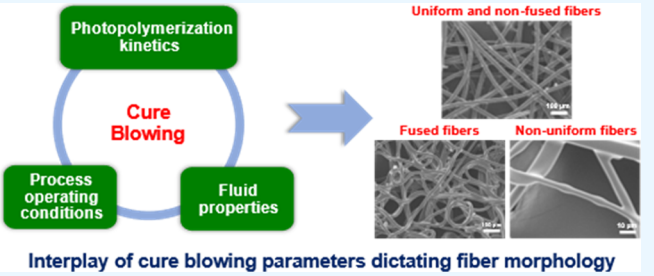

Interplay of cure blowing parameters dictating fiber morphology

KEYWORDS: *nonwovens, photopolymerization, cross-linking, vitrification, polymer processing*

INTRODUCTION

Nonwoven fibrous mats comprise randomly oriented fibers held together by physical entanglements and contact forces without weaving or knitting.[1] Nonwoven products currently constitute a $50 billion industry with an annual growth rate of ∼6%. The growth of the nonwovens industry can be attributed to a myriad of applications such as disposable medical and safety products,[2,3] catalytic and energy storage systems,[4,5] filtration media,[6−8] and tissue engineering scaffolds.[9,10] A few examples of very common nonwoven-based commodity products that society uses on a regular basis are absorbent media in diapers, scouring webs for kitchen cleaning, protective face masks and respirators, hospital gowns, filtration media in room air purifying and HVAC systems, and acoustic panels in automotive and aerospace industries. A majority of these applications rely on the lightweight, high specific surface area, and porous characteristics of these nonwoven mats. Since the extent of surface area per volume in a nonwoven mat varies inversely with the diameter ($A/V \sim 1/d$), technological advances in recent years have focused on enabling production of nonwoven mats comprising micron and submicron fiber sizes. A large number of companies, such as 3M, DuPont, Kimberly-Clark, Procter & Gamble, Freudenberg, Johns Manville, and Cummins, have a large portfolio of commercial products that leverage nonwovens technology.

Conventional nonwovens production techniques typically involve transforming a preformed, thermoplastic feed into a processable melt or solution state either by heating (e.g., melt spinning and melt blowing)[11,12] or by solvent addition (e.g., electrospinning).[1,8,13] The processable feed is subsequently drawn by an extensional force into liquid filaments, which solidify upon cooling below the polymer solidification temperature (e.g., a glass transition (T_g) or crystallization temperature (T_c)) or on rapid solvent evaporation. The large energy demands associated with these high-temperature processes and the volatile organic compound (VOC) emissions associated with added organic solvents have recently driven significant efforts to develop sustainable and environmentally friendly, nonwovens manufacturing processes. Moreover, commercial production of nonwovens using melt- and solution-based approaches are primarily limited to thermoplastic feedstocks, since thermosets cannot be easily transformed into a processable state. However, cross-linked thermoset nonwoven fibers are attractive targets since they offer superior thermal and chemical resistance with tailorable mechanical properties suitable for high-performance applications. For example, the high upper-service temperatures of

Received: May 22, 2023
Accepted: August 16, 2023
Published: September 6, 2023

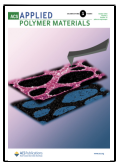

thermoset materials unlock applications of nonwovens as high-temperature filtration and catalyst-support media.

To address limitations of conventional fiber manufacturing techniques, we previously reported methods for producing cross-linked fibers by simultaneous spinning and photopolymerization of liquid monomers at ambient conditions using electrospinning[14−18] and centrifugal spinning.[19−21] In these studies, photoreactive mixtures of multifunctional liquid monomers were drawn into liquid fiber jets at room temperature containing little or no organic solvent using electrostatic or centrifugal forces, respectively, followed by rapid in-flight UV-initiated photopolymerization to yield solid fibers. Photopolymerization thus enabled formation of cross-linked fibers with tunable mechanical properties and excellent thermal and chemical stabilities.[16−18,21] Furthermore, the use of non-volatile liquid monomer mixtures obviates the requirements of high temperatures or organic solvents for fiber processing. However, electrospinning and centrifugal spinning are much less common in industrial nonwoven production. In contrast, micron-sized fibers produced by melt blowing processes constitute >10% of the global nonwovens market.[12] Therefore, the prospect of integrating UV photopolymerization with conventional melt blowing offers an attractive opportunity for producing cross-linked fibers in a more sustainable, high-throughput manner.

Recently, we reported the first "cure blowing" process to produce cross-linked nonwovens at room temperature by integrating in situ photopolymerization with a fiber spinning process closely resembling melt blowing.[22] During cure blowing, a photocurable liquid mixture comprising multifunctional thiol and acrylate monomers, free-radical photoinitiators, and viscoelasticity modifiers are extruded through a die orifice and drawn by ambient temperature, high-velocity air jets into liquid filaments. During flight toward a collector, the liquid filaments undergo rapid photo-cross-linking upon UV irradiation to generate solid, continuous, amorphous fibers. Preliminary studies revealed that the resulting fiber morphologies were governed by a convoluted, interdependent parameter space arising from the contributions of photopolymerization kinetics, monomer mixture fluid properties, and process operating conditions. For example, the interplay of process parameters such as air flow and monomer delivery rates, UV exposure time, and monomer mixture viscoelasticity triggered a fiber morphology transition from non-fused, uniform fibers to fibers with fused junctions and/or surface undulations at smaller diameters.[22] While formation of fused fibers stems from a competition between photopolymerization kinetics and UV exposure time, the onset of surface undulations arises from competing elastic and surface tension-driven stresses inherent to the viscoelastic liquid filament formed during fiber drawing. However, our studies indicated that analyses based only on the four aforementioned parameters do not fully describe the observed fiber morphology transitions. Therefore, a more thorough and comprehensive analysis is necessary to understand the fundamental origins of these fiber morphology transitions. Note that intentionally forming fiber mats with fused junctions may be beneficial in certain applications. Often, the as-processed nonwoven mats are subjected to chemical or thermal bonding processes to introduce fiber fusions in a controlled manner to improve the mat integrity and mechanical properties. Therefore, the ability to form fiber mats having fused junctions produced in a single step offers manufacturing advantages. A fundamental understanding of fiber morphology transitions is necessary to enable formation of fused junctions in an effective and reproducible manner.

A prior report by Fang et al. quantitatively analyzed the impact of different processing parameters on the resulting final fiber morphologies obtained by reactive centrifugal spinning in terms of three characteristic timescales: gel time, fluid relaxation time, and fiber flight time.[19] Since the interplay of photopolymerization kinetics and monomer mixture fluid properties central to reactive centrifugal spinning closely resembles that of cure blowing, their approach serves as a conceptual foundation for developing a detailed understanding of the fundamental principles of cure blowing. Notably, Fang et al. only examined a thiol-acrylate model system that reacts through mixed step- and chain-growth mechanisms.[19−21] However, other widely used photochemistries exhibit distinct photopolymerization mechanisms. For example, thiol-ene and (meth)acrylate photochemistries react exclusively by step-growth and chain-growth mechanisms, respectively.[25−30] Different photopolymerization mechanisms yield distinct cross-linked network characteristics, which translate into variable material properties. For instance, chain-growth systems typically yield higher modulus yet brittle materials, in contrast to more ductile, lower modulus materials obtained by similar step-growth systems. Implementation of different photochemistries may enable production of cross-linked fibers with tunable mechanical and physical properties suitable for a wider range of applications. However, the scope of the analysis developed by Fang et al. and its validity in different photopolymerization systems remain untested.[19]

Herein, we systematically and comprehensively investigate cure blowing fundamentals by extending the approach reported by Fang et al. for reactive centrifugal spinning.[19] We develop an analytical framework that describes the origins of fiber morphology transitions due to the different competing features of cure blowing irrespective of the photopolymerization mechanism of the monomer feed mixture, a key difference to the previous approach reported by Fang et al. The universality of this approach is investigated in the context of two reactive model systems, thiol-acrylate and thiol-ene chemistries, which photopolymerize by mixed step- and chain-growth and exclusively step-growth mechanisms, respectively. Thiol-acrylate polymerization involves reaction of thiyl radicals that add across the C═C bond of acrylates to generate carbon radicals that can react with other −SH groups in a step-growth manner or undergo a chain-growth reaction with other C═C acrylate groups.[23,24] In contrast, thiol-ene polymerization only involves step-growth reactions between thiyl radicals and C═C functional groups because the C═C bonds cannot undergo chain-growth reactions with carbon radicals.[25−28] To elucidate the origins of fiber morphology transitions, the interplay of process parameters related to the photopolymerization kinetics, monomer mixture fluid properties, and process operating conditions is quantified and compared using morphology maps constructed in terms of the characteristic timescales inherent to cure blowing.

EXPERIMENTAL SECTION

Materials. Dipentaerythritol pentaacrylate (DPPA, contains ≤650 ppm MEHQ inhibitor), pentaerythritol tetrakis(3-mercaptopropionate) (PETT, >95%), 1,3,5-triallylisocyanurate (TAIC, 98%), poly(ethylene oxide) (PEO, M_v = 10^6 g/mol), and ethyl acetate (anhydrous, 99.8%) were purchased from Millipore-Sigma. Omnirad

https://doi.org/10.1021/acsapm.3c01083
ACS Appl. Polym. Mater. 2023, 5, 7841−7853

2100 (a mixture of 90−95 wt % ethyl phenyl(2,4,6-trimethylbenzoyl)-phosphinate and 5−10 wt % phenyl bis(2,4,6-trimethylbenzoyl)-phosphine oxide) was provided by IGM Resins. All chemicals were used as received. The chemical structures of the monomers and photoinitiator are provided in Figure 1.

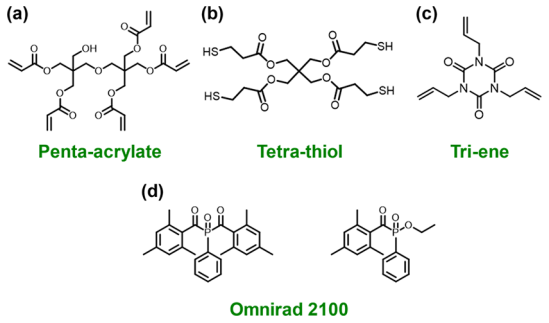

Figure 1. Chemical structures of the reactive monomers and photoinitiator. (a) Dipentaerythritol pentaacrylate (DPPA), (b) pentaerythritol tetrakis (3-mercaptopropionate) (PETT), (c) 1,3,5-triallylisocyanurate (TAIC), and (d) Omnirad 2100: composed of 90−95 wt % of ethyl phenyl (2,4,6-trimethylbenzoyl)-phosphinate (left) and 5−10 wt % of phenyl bis(2,4,6-trimethylbenzoyl)-phosphine oxide (right).

Monomer Feed Mixture Preparation. A specified amount of PEO was first dissolved in PETT at 80 °C for 4 h. PETT was chosen since its lower viscosity aids complete PEO dissolution. This mixture was then added to a predetermined amount of DPPA (or TAIC), maintaining a constant molar ratio between thiol and acrylate functional groups (or thiol and ene functional groups). Finally, requisite amounts of ethyl acetate and the photoinitiator (Omnirad 2100) were added, followed by vortex mixing for 5 min. Ethyl acetate serves as a nonreactive diluent to modify the monomer mixture viscosity, while trace amounts of high molecular weight PEO acts as an elasticity modifier to enhance the elastic properties of the monomer mixture without significantly altering its viscosity. Omnirad 2100 was used as the free-radical photoinitiator, primarily due to its 365 nm peak absorbance wavelength that matches the output spectrum of the light source. A typical DPPA−PETT monomer mixture comprised 64 wt % DPPA, 19 wt % PETT, 5 wt % Omnirad 2100, and 12 wt % ethyl acetate. Similarly, a typical TAIC−PETT monomer mixture comprised 37 wt % TAIC, 54 wt % PETT, 5 wt % Omnirad 2100, and 4 wt % ethyl acetate. In both cases, the PEO content was maintained at 500 ppm based on the total mass of the reactive monomers, unless otherwise noted. The prepared mixture was then loaded into a 5 mL syringe masked with a black tape to avoid premature cross-linking by stray light during fiber spinning. All these steps were performed in a room with overhead light filtering to further minimize the effects of ambient light during sample preparation.

Cure Blowing Apparatus. A schematic of the lab-scale cure blowing apparatus is shown in Figure 2 (see ref 22 for additional details).[22] In this study, the monomer delivery rate was modulated from 0.075 to 0.25 mL/min while the air flow rate was varied from 0.5 to 2 standard cubic feet per minute (SCFM), which translates to an air velocity of 32 to 155 m/s at the die face. The distance between the die face and the edge of the illuminated region was maintained at 4 cm. As illustrated in Figure 2, two UV-grade mirrors (Thorlabs, Inc.) with an average reflectance >90% over the range λ = 250−450 nm provided additional reflected light to drive photopolymerization. The effective incident light intensities (i.e., incident + reflected) for cure blowing experiments using the thiol-acrylate and thiol-ene model systems were maintained at 1.4 and 1 W/cm^2, respectively, in the same plane as the fiber path as measured by a FieldMaxII radiometer (Coherent, Inc.). The actual light intensities in the fiber path plane were measured by a radiometer both before and after reflection from the mirrors to account for the loss of light intensities upon reflection and accurately determine the effective light intensities. The composite light spot formed at the plane of the fiber path was approximately 12 cm in length.

Time-Resolved Fourier Transform Infrared Spectroscopy. Photopolymerization kinetics of thiol-acrylate and thiol-ene monomer mixtures were studied by time-resolved Fourier transform infrared (TR-FTIR) spectroscopy using a Thermo Fisher Scientific Nicolet 6700 FTIR spectrometer equipped with a KBr beam splitter and MCT-A detector in rapid scan mode. To minimize effects of ambient light, a drop of freshly prepared monomer mixture was spin-coated onto a NaCl window to obtain a thin film in a room with overhead light filtering ("an orange-lighted room"). This sample was loaded into the spectrometer using a custom-made horizontal transmission accessory. The sample was continuously purged with zero-grade air and a series scan was taken under ambient conditions with a time resolution of 0.04 s and a spectral resolution of 14.73 cm^{-1}. Each sample was allowed to rest within the FTIR accessory with no light exposure for ∼30 s, after which the light source was activated. The same light source as that used for fiber spinning experiments was used for TR-FTIR studies. The fractional conversions of C═C double bonds in both the model monomer feed mixtures were quantified by the reduction in areas of the acrylate double bond stretching (1630 cm^{-1}) and ene vinylic hydrogen stretching (3115 cm^{-1}) peaks during UV illumination.[23−25] The double bond conversion was then calculated by

$$\%\text{conversion} = \frac{A_0 - A_t}{A_0} \times 100 \quad (1)$$

where A_0 and A_t are the respective peak areas at t = 0 s (prior to light exposure) and at a given UV irradiation time.

Dynamic Mechanical Analysis. The glass transition temperature (T_g) evolution of partially cured thermosets was measured with a TA Instruments RSA-G2 solids analyzer using the tension geometry. Temperature sweeps were conducted at a frequency ω = 1 Hz, strain $|\gamma|$ = 1%, and a heating rate of 3 °C/min to obtain the loss tangent (tan δ) as a function of temperature. The temperature corresponding

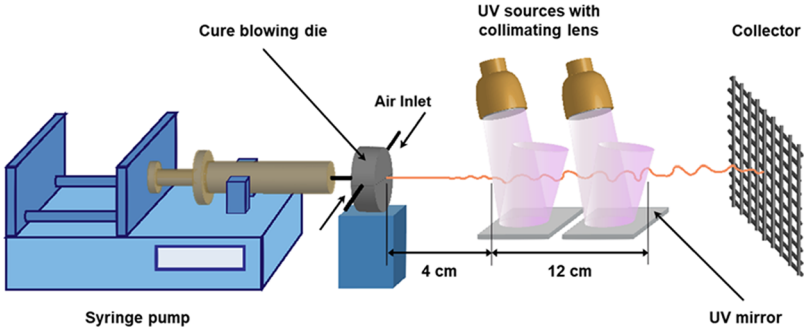

Figure 2. Schematic representation of the lab-scale cure blowing apparatus used in this study.

https://doi.org/10.1021/acsapm.3c01083
ACS Appl. Polym. Mater. 2023, 5, 7841−7853

to the peak in the tan δ curve was taken as T_g. Heating was stopped as soon as the tan δ peak was observed to minimize additional thermal curing during the temperature sweep studies. Consequently, the T_g measured in a second heating scan was never observed to deviate more than ∼5−7 °C from the T_g measured in the first heating scan. Additionally, temperature changes of monomer mixture films during photopolymerization due to the reaction exotherm were measured using an MT-29/1HT Needle Microprobe (Physitemp Instruments) attached to a Microtherma 2 High Precision Type T Thermocouple Meter (ThermoWorks).

Capillary Breakup Extensional Rheometry and Shear Rheometry. Viscosities of the monomers and their mixtures were measured with a stress-controlled AR-G2 rheometer (TA Instruments, Inc.). Steady-state shear experiments were performed using a parallel-plate geometry with a 40 mm diameter upper plate on a Peltier lower stage at 25 °C. Steady-state shear viscosities were measured over the range of shear rates $\dot{\gamma}$ = 0.1−100 s^{-1}. The elastic nature of the monomer feed was characterized using a CaBER 1 capillary breakup extensional rheometer (HAAKE) equipped with 4 mm diameter parallel plates.[31] A laser micrometer with 1000 Hz resolution recorded the filament diameter evolution produced by a step stretch. The fluid relaxation time was determined by fitting the exponential decay of the filament diameter using the elastic fluid mode.[31,32] The photoinitiator was not added to the monomer mixtures to avoid unwanted curing under ambient light during measurements. We assumed that the low photoinitiator content (≲5 wt %) does not considerably alter the monomer mixture viscoelasticity. Monomer mixture samples were immediately characterized after preparation.

Scanning Electron Microscopy and Visible Light Microscopy. Cure blown fibers were imaged with a Nikon Optiphot visible light microscope (VLM) equipped with a Canon SL1 digital camera and a Hitachi S-4700 FE-SEM. For VLM, the fiber samples were sandwiched between two glass slides and imaged in transmission light illumination mode. For FE-SEM, the fiber samples were coated with an ∼7 nm layer of iridium using an ACE600 Coater prior to imaging.

RESULTS AND DISCUSSION

Parameters Governing Cure Blowing. From the cure blowing apparatus shown in Figure 2, the key processing steps are: (i) extrusion of the photoreactive monomer mixture feed through the die, (ii) rapid liquid filament drawing by ambient temperature high-velocity air jets, (iii) solidification of the liquid fiber during flight by UV-initiated photopolymerization and cross-linking, and (iv) fiber collection. Each step crucially depends on several parameters that collectively regulate the final fiber characteristics. Table 1 lists the control parameters in cure blowing, which may essentially be grouped into three major categories representing: (i) monomer chemistry and reactive feed composition that specify the underlying photopolymerization kinetics, (ii) monomer mixture fluid properties that governs the formation and stability of the liquid filament, and (iii) process operating conditions, such as the air flow rate and monomer delivery rate, that influence the extent of fiber drawing and fiber flight time. These three categories of parameters are also interrelated in a convoluted manner. For example, changing the functionality and/or the molar ratio of the monomers affects both the photopolymerization kinetics and the viscoelastic properties of the reactive monomer mixture. Furthermore, the interplay of the categories of parameters vitally dictates the final fiber morphology. For example, Figure 3a,b highlights a morphology transition from non-fused fibers to fibers with significantly more fused junctions at higher air flow rates; the latter conditions correspond to shorter UV exposure times. The onset of fiber fusion arises from an imbalance between the photopolymerization kinetics (i.e., the time necessary for sufficient photo-cross-linking) and process operating conditions (i.e., the UV exposure time available during cure blowing). As a result, incompletely cured fiber surfaces predominate and are susceptible to uncontrolled, random fiber fusion after deposition at the collector. Additionally, Figure 3a,c reveals another type of morphology transition from uniform to non-uniform fiber diameters that is characterized by periodic surface undulations upon reduction of the PEO elasticity modifier content in the monomer feed. The onset of surface undulations stems from surface tension-driven stresses that overwhelm the opposing extensional stresses inherent in the viscoelastic liquid fiber. If sufficient elastic properties are not imparted to the liquid monomer mixture by adding small amounts of a high molecular weight PEO, the growth of surface instabilities becomes unavoidable during liquid fiber flight prior to photopolymerization and solidification. As a result, periodic surface undulations and even "beads-on-string" morphologies appear and can be arrested by covalent bond formation and cross-linking.

Table 1. Classification of Cure Blowing Processing Parameters

photopolymerization kinetics	monomer mixture fluid properties	process operating conditions
monomer functionality	viscosity	UV dosage
molar ratio of monomers	elasticity	air flow rate
monomer reactivity	surface tension	monomer delivery rate
UV dosage		die geometry

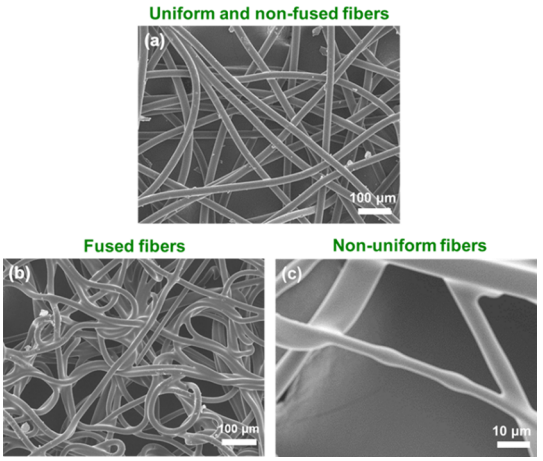

Figure 3. Representative SEM images showing the transition of fiber morphology from (a) non-fused to (b) fused fibers on increasing the air flow rate from 0.5 to 1.5 SCFM and (a) uniform to (c) non-uniform fiber diameters on reducing PEO elasticity modifier content in the monomer feed mixture from 760 to 300 ppm.

The aforementioned fiber morphology transitions exemplify the critical competition between the three categories of parameters that dictate the final cure blown fiber morphology. One way to better quantify these competing features is to condense the contributions of each category of parameters in Table 1 into their respective characteristic timescales. Consequently, combinations of these characteristic timescales can essentially describe the entire cure blowing process, while

https://doi.org/10.1021/acsapm.3c01083
ACS Appl. Polym. Mater. 2023, 5, 7841−7853

order-of-magnitude comparisons between them may also provide further insights into the origins of the observed fiber morphology transitions. The following sections introduce the relevant timescales for each category of parameters, along with the characterization methods used for their estimation.

Photopolymerization Kinetics and Vitrification Time. Photopolymerization kinetics are a critical aspect of cure blowing, since sufficient photo-cross-linking of the liquid fiber jet during flight is crucial to obtaining well-cured, uniform fibers. The photopolymerization kinetics depend on system-specific variables, such as monomer functionality and reactivity, molar ratio of the thiol and ene functional groups, UV dose, and photoinitiator content (Table 1). The monomer identity is also a key factor since it dictates the photopolymerization mechanism. Photopolymerizations typically occur through three types of mechanisms: pure chain-growth (e.g., (meth)-acrylates)),[29,30] pure step-growth (e.g., thiol-ene and thiol-yne),[26,27,33,34] and mixed step- and chain-growth (e.g., thiol-acrylate).[23−25,35] Each mechanism translates into a distinct cross-linked network topology. For example, pure chain-growth networks produced by (meth)acrylate monomers form by rapid chain-extension reactions leading to a more heterogenous network with a high cross-link density and a wide distribution of chain lengths between cross-links.[30,36,37] In contrast, pure step-growth networks exhibit successive propagation and chain-transfer reactions that generate a more homogenous network with uniform chain lengths between cross-links.[18,26] Notably, distinct network evolution mechanisms are expected to produce different extents of liquid fiber jet solidification during in situ photopolymerization, in turn impacting the final morphology of cure blown fibers. In this study, we focused on thiol-acrylate and thiol-ene model systems, which exhibit mixed step- and chain-growth and pure step-growth mechanisms, respectively.

A commonly used parameter to describe the evolution of a cross-linked network during photopolymerization is the gel point.[33,35] The gel point is defined as the critical extent of the reaction at which a continuous, infinite network first appears, and the polymerization time required to reach the gel point is defined as the gel time. For a mixed chain- and step-growth polymerized network, the gel point in terms of fractional conversion of the acrylate C═C bonds, p_α, can be calculated from the following equation:[15,35]

$$\frac{2}{r}(f_{\text{acrylate}} - 1)\frac{k_{CC}}{k_{CS}}p_\alpha + (f_{\text{acrylate}} - 1)(f_{SH} - 1)\left(1 + \frac{1}{r}\frac{k_{CC}}{k_{CS}}\right)p_\alpha^{\,2} = 1 \tag{2}$$

where $r = [-SH]/[C{=}C]$, f_{acrylate} and f_{SH} are the acrylate and thiol monomer functionalities, respectively, and k_{CC}/k_{CS} is the ratio of the propagation rate constant for acrylate homopolymerization to the acrylate-to-thiol chain-transfer rate constant, which is reported to be ∼1.5.[23] In this study, the thiol to acrylate functional group molar ratio was maintained at [−SH]:[C═C] = 1:4. Previous reports have demonstrated that for the selected thiol and acrylate monomers, this 1:4 molar ratio suppresses oxygen inhibition without noticeably slowing the reaction kinetics.[14] Moreover, the 1:4 molar ratio of thiol to acrylate functional groups leads to approximately equal rates of consumption of both functional groups, which is an assumption in the derivation of eq 2.[38] Excess of acrylate functional groups are necessary since they participate in both chain-growth and chain-transfer reactions, whereas thiol groups only participate in chain-transfer reactions.

For networks derived from a pure step-growth mechanism, the gel point in terms of the fractional conversion of C═C bonds, p_α, can be calculated using the Flory−Stockmayer equation:[33]

$$p_\alpha = \frac{1}{\sqrt{r(1 - f_{\text{ene}})(1 - f_{SH})}} \tag{3}$$

where $r = [-SH]/[C{=}C]$ and f_{ene} and f_{SH} are the ene and thiol monomer functionalities, respectively. A value of $r = 1$ was maintained, since the inability of the ene functionality to undergo chain-growth ensures equal rates of consumption of both functional groups during chain-transfer polymerization.[18,26,39]

Using eqs 2 and 3, the p_α values for the thiol-acrylate and thiol-ene model systems were, respectively, calculated to be ∼2% of the acrylate conversion and ∼41% of ene conversion. The considerable delay in gelation (higher p_α) for thiol-ene photochemistry is attributed to the pure step-growth mechanism; the absence of a rapid chain-growth reaction delays the first appearance of an infinite cross-linked network. The thiol-acrylate and thiol-ene photopolymerization kinetics were monitored using TR-FTIR (see the Experimental Section for details). In the remaining discussion, reaction conversion for either model systems refers to the C═C double bond conversion therein. The conversion versus time data and calculated p_α values were used to estimate the respective gel times (t_{gel}) corresponding to the light intensities used in cure blowing. The t_{gel} values for the thiol-acrylate and thiol-ene systems were estimated to be ∼3 and ∼35 ms, respectively. The detailed procedure for t_{gel} estimation using TR-FTIR has been reported previously and is also provided in the Supporting Information.[19,22] Intuitively, the delayed gel time of the thiol-ene system suggests that difficulties could arise in obtaining well-cured fibers from cure blowing. However, the thiol-ene monomer mixture could be readily cure blown, and it exhibited a similar morphology transition as in the aforementioned thiol-acrylate system. These observations suggest that t_{gel} may not be an appropriate timescale for describing cure blown fiber morphology transitions of monomer feeds that operate by different photopolymerization mechanisms. Therefore, an alternative timescale must be considered to account for differences in the photopolymerization characteristics of cross-linked networks evolving through distinct mechanisms. Note that, since Fang et al. studied only a thiol-acrylate model system, the necessity of an alternative timescale instead of the gel time was not apparent nor considered.[19]

A closer look at the typical sequence of network evolution during photopolymerization (Figure 4) for model systems with cured-state glass transition temperatures (T_gs) above room temperature reveals that the reactive monomer mixture undergoes two major network development events, gelation and vitrification.[29,40,41] At the gelation point, liquid monomers transform into a rubbery gel phase that fixes the fibrillar shape. At this point, significant amounts of unreacted functional groups remain (∼98% for thiol-acrylate and ∼59% for thiol-ene) that continue to react and further develop the cross-linked network. However, network densification in the postgelation state is associated with reductions in the free

https://doi.org/10.1021/acsapm.3c01083
ACS Appl. Polym. Mater. 2023, 5, 7841−7853

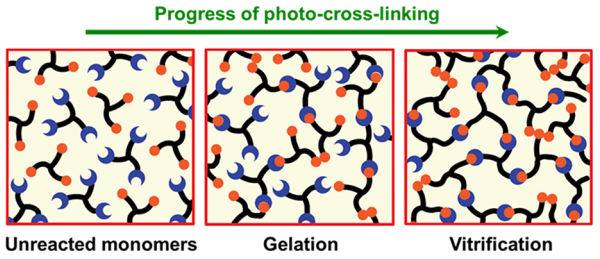

Figure 4. (a) Schematic representation of the network growth during photopolymerization of a thiol-acrylate model system where unreacted liquid monomers (left) progress through gelation (middle) and vitrification (right) events to yield a solid, cross-linked network.

volume and mobilities of the unreacted functional groups. At the vitrification point, the mobility restriction of the unreacted functional groups reaches a critical point where photopolymerization becomes severely diffusion-limited. Consequently, further cross-linking cannot occur since the residual functional groups essentially remain trapped within the network. Thus, vitrification marks the transformation of the rubbery phase to a glassy state.[41,42] Note that for model systems with cured-state T_g below room temperature, the transition into a glassy state is likely to be dominant over gelation characteristics. For the thiol-acrylate and thiol-ene model systems reported in this study, vitrification drives the transition of the cross-linked network into a glassy state. Therefore, the diffusion-limited trapping of unreacted functional groups in the glassy state is unavoidable for the experimental conditions in our studies. In this glassy network state, the trapped functional groups do not have the ability to migrate to the fiber surface. However, it has been widely reported that if a partially cross-linked network is subsequently heated beyond its T_g, the diffusion-limitation effect reduces and remaining functional groups may further cross-link upon appropriate reaction reinitiation.

Evolution of the cross-linked network can be correlated experimentally with the photopolymerization kinetics by tracking the change in the conversion rate as a function of the fractional conversion for the thiol-acrylate and thiol-ene model systems (Figure 5).[29,43,44] The progression of photopolymerization may be divided into three distinct reaction regimes: autoacceleration, autodeceleration, and severe diffusion-limitation. At early reaction times, a sharp increase in the conversion rate was observed, which is attributed to the dominance of free-radical initiation and propagation over termination reactions. The reduced mobility of the growing chains impedes radical termination while the significantly higher mobility of the smaller monomers results in an autoacceleration phenomenon known as the "Trommsdorff effect".[36,40,43−45] Network gelation in this regime also contributes to this autoacceleration effect. At some point after gelation, the continuing network densification concomitantly reduces the mobility of the reactive monomers leading to slower radical propagation that manifests as a conversion rate maximum. Moreover, Figure 5 reveals that the magnitude of the conversion rate maximum for the thiol-ene system is ∼6 times that of the thiol-acrylate system. This observation is corroborated by previous reports by Reddy et al., which revealed greater propagation and chain-transfer reaction constants for the thiol-ene photochemistry ($k_p \sim 2.1 \times 10^6$ L/mol s, and $k_{ct} \sim 2.1 \times 10^5$ L/mol s) as compared to the propagation, chain-transfer, and chain-growth reaction constants for thiol-acrylate photochemistry ($k_p \sim 1.2 \times 10^6$ L/mol s, $k_{ct} \sim 0.8 \times 10^5$ L/mol s, and $k_{cg} \sim 1.1 \times 10^5$ L/mol s).[25] Thus, a faster photopolymerization rate was observed for the thiol-ene model system despite the ene monomer being trifunctional compared to the pentafunctional acrylate. Beyond this peak in the conversion rate, the photopolymerization gradually becomes diffusion-controlled, resulting in a deceleration of the rate of photopolymerization.[43−45] Finally, the third regime marks the onset of vitrification where the conversion rate rapidly approaches zero as severe diffusion-limitations in the cross-linked network restrict further reactions of residual functionalities.[43−45] Notably, Figure 5 indicates that the conversion rate maximum and the onset of vitrification were both observed at a higher C═C conversion for the thiol-ene system. This observation may be attributed to the delayed gelation of the step-growth network formed in the thiol-ene system (∼41% C═C conversion) as compared to the early gelation in the thiol-acrylate system (∼2% C═C conversion) due to the additional chain-growth reactions. Consequently, mobility restrictions for the unreacted monomers develop later in a step-growth network, thereby allowing the photopolymerization to proceed to a higher conversion.

Evolution of the network during photo-cross-linking suggests that cure blown fibers exhibiting fused junctions are likely photopolymerized beyond the gel point, thus maintaining their fibrillar shapes. However, they lack a sufficiently high conversion to have vitrified into solids and thus the mobilities of the residual monomers near the fiber surfaces enable formation of fused junctions after deposition on a collector. In

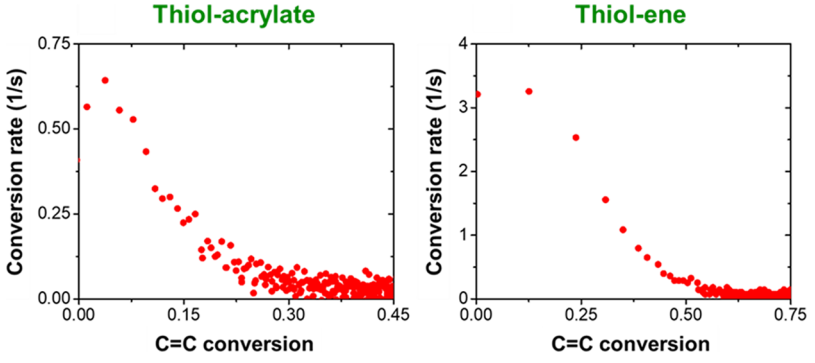

Figure 5. Conversion rate as a function of C═C fractional conversion obtained from TR-FTIR studies during the photopolymerization of (left) thiol-acrylate and (right) thiol-ene model systems. Both photopolymerizations were performed at a light intensity of 5 mW/cm^2 using monomer mixtures containing a 6 wt % photoinitiator.

https://doi.org/10.1021/acsapm.3c01083
ACS Appl. Polym. Mater. 2023, 5, 7841−7853

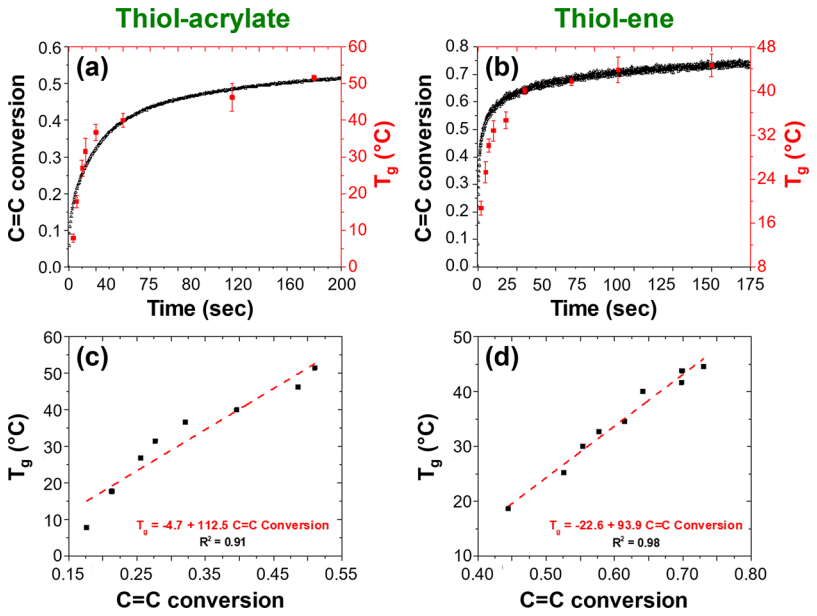

Figure 6. Evolution of T_g and C═C conversion with time at a light intensity of 5 mW/cm^2 and a photoinitiator content of (a) 1.5 wt % for the thiol-acrylate and (b) 0.5 wt % for the thiol-ene model systems. (c, d) displays the variation of T_g with C═C conversion and the corresponding linear fit equations obtained by replotting the T_g and C═C conversion versus time data shown in (a, b).

contrast, non-fused fibers are likely vitrified where the residual functional groups are trapped within the cross-linked network, thereby preventing further reaction that would have caused fiber surface fusion on contact. Therefore, the vitrification time may be a more appropriate timescale for representing the photopolymerization parameters that underly the non-fused to fused fiber morphology transition.

While the gel point is well defined in terms of the relevant kinetic parameters in eqs 2 and 3, the onset of vitrification depends on parameters such as light intensity, monomer mixture composition, etc., since they regulate the extent of mobility restrictions encountered by the evolving network during photo-cross-linking. Thus, it is extremely difficult to apply a theoretical treatment to accurately estimate a phenomenological event such as vitrification. In this study, we used T_g of the evolving network to estimate the vitrification times for both thiol-acrylate and thiol-ene model systems.[46−48] With advancing photopolymerization, growth of a network translates into an increasing T_g. At the vitrification point, T_g of the cross-linked material exceeds the curing temperature (T_{cure}), since $T_{cure} < T_g$ implies that the cross-linked network transforms into a glassy state that kinetically traps the reactive species to prevent further cross-linking. Similar correlations between T_g and the vitrification point are also well-known for thermally initiated cross-linked networks such as epoxy-amine and epoxy-anhydride thermosets.[49−52]

We developed a strategy utilizing a powerful combination of dynamic mechanical analysis (DMA) and TR-FTIR to monitor the evolution of T_g and correlate it with the C═C double bond conversion in monomer mixture films to estimate the vitrification times. However, to obtain a well-resolved time evolution of T_g and C═C conversion, DMA and TR-FTIR experiments were performed at lower light intensities and photoinitiator loadings in the cure blowing monomer mixtures of both model systems to slow the photopolymerization reactions. While the light intensity was maintained at 5 mW/cm^2, the photoinitiator contents were adjusted to 1.5 wt % for thiol-acrylate and 0.5 wt % for thiol-ene systems such that the T_g of the cured film is similar to the T_g of the cure blown fiber mats, implying similar final network configurations. This ensures comparable network evolution for the film and fiber curing geometries. Approximately 100 μm thick films of the reactive monomer mixtures of both model systems were coated onto silicone strips as a support and photopolymerized for different durations. The partially cured bilayer films were then attached to the DMA clamps and oscillatory experiments were conducted to measure the loss tangent (tan δ) as a function of temperature (see Figure S1 for a schematic representation of the experimental geometry). The temperature corresponding to the peak of the tan δ curve was taken as the T_g of each partially cured specimen.[46] Figure 6a,b simultaneously shows the time-dependent evolution of T_g and the C═C conversion during photopolymerization for the thiol-acrylate and thiol-ene systems. Figure 6a,b may be replotted to directly correlate T_g with conversion as shown in Figure 6c,d, which shows that the T_g versus conversion data fits relatively well to a linear equation. The better quality of fit for the thiol-ene system (Figure 6d) may be attributed to the more homogenous network of a purely step-growth system, in contrast to the heterogenous nature of a thiol-acrylate network (Figure 6c). The conversion corresponding to the vitrification point for both model systems can be determined from the T_g versus conversion relation as the point at which $T_g = T_{cure}$. However, the exothermic nature of free-radical polymerizations causes the internal temperature to exceed the ambient temperature and the maximum temperature is taken as T_{cure}.[50] To determine T_{cure}, the temperature evolutions of both model systems during photopolymerization were monitored using a needle microprobe embedded in the uncured films of the monomer mixtures. T_{cure} values for the thiol-acrylate and thiol-ene systems were thus determined to be 40 and 34 °C, respectively. From the linear fits shown in Figure 6c,d, the conversions at vitrification corresponding to the measured T_{cure} values were estimated to be ∼39 and ∼60% for the thiol-acrylate and thiol-ene model systems, respectively. The higher vitrification conversion for the thiol-ene system is supported by

https://doi.org/10.1021/acsapm.3c01083
ACS Appl. Polym. Mater. 2023, 5, 7841−7853

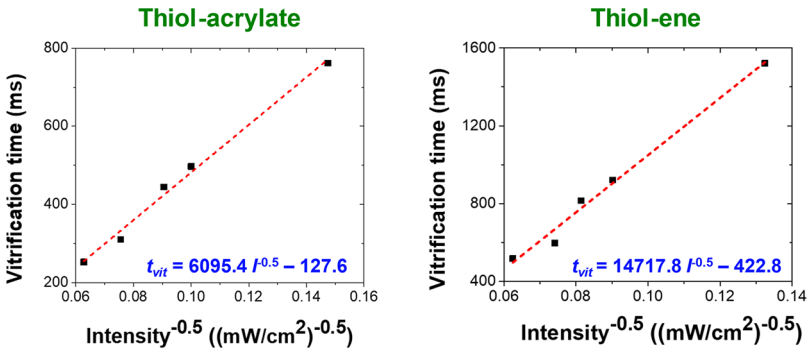

Figure 7. Vitrification time as a function of light intensity obtained from the photopolymerization kinetics of (left) thiol-acrylate and (right) thiol-ene model systems. The dashed lines represent the linear fit of the displayed data.

the earlier observation on the evolution of the conversion rate with the progress of photopolymerization (Figure 5).

The DMA and TR-FTIR analyses discussed above were performed at much lower light intensity and photoinitiator contents compared to the cure blowing experiments. Therefore, the vitrification point data must be appropriately extrapolated to estimate the vitrification times (t_{vit}) for both model systems at the actual process operating conditions. Note that the final T_g of cross-linked thermosets photopolymerized at a constant light intensity were observed to be similar irrespective of the photoinitiator content. Therefore, the estimated vitrification point values can be reasonably expected to be invariant of the photoinitiator content in the monomer mixture since T_g of a cross-linked network is a direct manifestation of the conversion of the reactive groups. The extrapolation analyses required additional TR-FTIR measurements to ascertain the dependence of the photopolymerization kinetics on the light intensity for proper extrapolation. TR-FTIR studies were performed at lower light intensities ranging from 38 to 250 mW/cm^2 while maintaining a photoinitiator content of 5 wt % (same as the cure blowing experiments) for both thiol-acrylate and thiol-ene systems to obtain a well-resolved time-dependent evolution of C═C conversion. For conventional free-radical polymerizations with bimolecular termination, the rate of polymerization (R_p) scales with the rate of initiation (R_i) as $R_p \propto (R_i)^{1/2}$. For the photopolymerization chemistries used in this study, the initiation rate is directly proportional to the light intensity ($R_i \propto I$).[30] Therefore, at the vitrification point (i.e., at a specific change in the monomer concentration), t_{vit} is proportional to $I^{-1/2}$. Figure 7 shows the variation of t_{vit} values as a function of $I^{-1/2}$ and the resulting linear fit equations that were used to estimate t_{vit} at the process light intensities. The t_{vit} values for the thiol-acrylate and thiol-ene systems were estimated to be 30 and 42 ms, respectively. Table 2 summarizes the results obtained from the gelation and vitrification analyses of both thiol-acrylate and thiol-ene model systems. In summary, the category of parameters dictating the photopolymerization kinetics was best quantified in terms of the vitrification time. Analyses based on the two reactive model systems that exhibit distinct network evolution mechanisms revealed that the previous understanding of the relation between the photopolymerization kinetics and photopolymerized fiber morphology in terms of the gel time is not universally valid. Comparison with other characteristic timescales in the subsequent sections will further highlight the validity of vitrification time as the relevant photopolymerization timescale irrespective of the reaction mechanism (vide infra).

Table 2. Summary of Gelation and Vitrification Analyses in Thiol-Acrylate and Thiol-Ene Cure Blowing Model Systems

	thiol-acrylate	thiol-ene
process light intensity	1.4 W/cm^2	1.0 W/cm^2
T_{cure}	40 °C	34 °C
gel point	2% C═C conversion	41% C═C conversion
gel time	3 ms	35 ms
vitrification point	39% C═C conversion	60% C═C conversion
vitrification time	30 ms	42 ms

Monomer Mixture Viscoelasticity and Fluid Relaxation Time. The category of parameters corresponding to the viscoelasticity of the monomer mixture feed also plays a key role in dictating cure blown fiber morphology. In this study, ethyl acetate was used as a nonreactive diluent to obtain a homogenous monomer mixture and regulate the viscosity to ensure extrusion and drawing of the monomer feed into liquid fiber jets. Notably, ethyl acetate can also be replaced with nonvolatile reactive diluents, such as 1,6-hexanediol diacrylate, *N*-vinylpyrrolidone, butyl acrylate, etc., to eliminate VOCs. Additionally, a trace amount of high molecular weight PEO (125−760 ppm) was added to the monomer mixture as an elasticity modifier. Our initial studies demonstrated the critical role of monomer mixture elasticity to facilitate drawing of liquid fiber jets and to suppress the surface tension-driven Rayleigh instabilities inherent to the elongated liquid jets prior to in-flight photopolymerization.[22,53−55] Fluid instabilities in liquid fiber jets with insufficient extensional properties manifest as periodic surface undulations and necking along the fiber axis, which in extreme cases may cause complete breakup into droplets.[31,56−58]

The extensional properties of the monomer mixtures may be quantified by their characteristic fluid relaxation timescales, as measured by capillary breakup extensional rheometry (CaBER). CaBER, which is commonly used to study low viscosity viscoelastic fluids (η < 1 Pa s), measures the elastic response of a viscoelastic liquid filament to a capillary stress-driven uniaxial extensional flow by tracking the time evolution of the filament diameter.[59−61] Figure 8 shows that the liquid filaments generated from the monomer mixtures of both model systems undergo rapid breakup in the absence of any resisting extensional stresses within the filament (0 ppm lines). In comparison, the addition of trace amounts of high MW PEO enhances the elasticity of the monomer mixture such that the resulting extensional stresses developed within the self-

https://doi.org/10.1021/acsapm.3c01083
ACS Appl. Polym. Mater. 2023, 5, 7841−7853

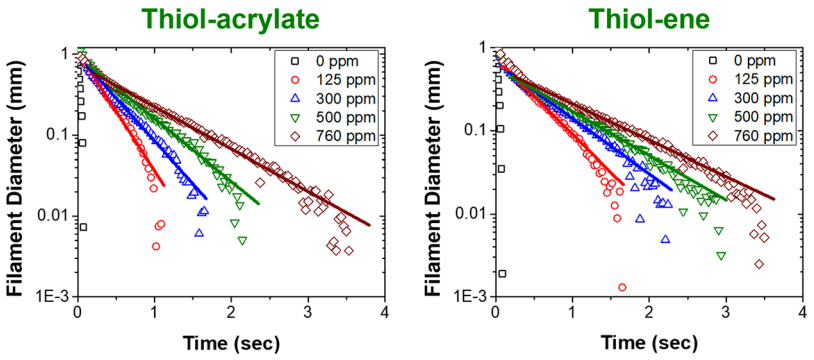

Figure 8. Evolution of the filament diameter during surface tension-driven self-thinning of the filaments generated from the monomer mixtures of (left) thiol-acrylate and (right) thiol-ene model systems containing 760 ppm (diamond), 500 ppm (inverted triangle), 300 ppm (triangle), 125 ppm (circle), and 0 ppm (square) PEO, respectively. The solid lines represent the fits to the elastic fluid model.

thinning filament can resist breakup for longer durations of time. The exponential thinning of the filament can be described by the elastic fluid model shown in eq 4, which is obtained from the balance between the elasto-capillary stresses in the liquid filament.[31,61,62]

$$D(t) = D_0\left(\frac{D_0 G}{4\sigma}\right)^{1/3} e^{-t/3\lambda_c} \quad (4)$$

where $D(t)$ is the time-dependent filament diameter measured by a laser micrometer in CaBER, D_0 is the initial filament diameter, G is the elastic modulus, σ is the surface tension, and λ_c is the characteristic relaxation time of the monomer mixtures. The characteristic fluid relaxation times of the monomer mixtures were extracted by fitting eq 4 to the exponential region of the diameter decay profiles shown in Figure 8. Table 3 lists the estimated fluid relaxation time values as a function of the PEO content for both thiol-acrylate and thiol-ene model systems.

Table 3. Summary of the Fluid Relaxation Times of Model Cure Blowing Monomer Mixtures as a Function of PEO Additive Content

	fluid relaxation time (ms)	
PEO content (ppm)	thiol-acrylate	thiol-ene
760	214	337
500	187	269
300	137	216
125	101	158

Note that the filament thinning in CaBER is solely driven by surface tension, whereas liquid fiber drawing in cure blowing involves a considerable additional contribution from the drag force imparted by the high-velocity air jets. Therefore, the extensional rates encountered during cure blowing are expected to be significantly higher than that achievable from CaBER. Nevertheless, CaBER analysis still provides a semi-quantitative evaluation of the transient viscoelastic response of a rapidly thinning filament. The estimated fluid relaxation time can be compared with other characteristic timescales to gain insights into the transition of cure blown fiber morphology from uniform to non-uniform fiber diameters.

Process Operating Conditions and Fiber Flight Times. The two relevant fiber flight timescales that govern fiber morphology in cure blowing are: (i) flight time to the light spot and (ii) UV exposure time. The flight time to the light spot is the time taken by the liquid fiber jet to travel from the die face to the edge of the UV irradiation spot. In contrast, the UV exposure time represents the duration of time the fiber jet spends in the light spot, which is essentially the time available for liquid fiber jet photopolymerization and solidification prior to reaching the collector. Both fiber flight times may be directly estimated from the air and fiber jet velocities used in cure blowing and the location and size of the light spot.

Earlier studies investigated air velocity and fiber velocity profiles in melt blowing both experimentally and theoretically using die configurations closely resembling the cure blowing die used in this study.[63−68] Therefore, the general characteristics of the velocity profiles observed in melt blowing can be reasonably expected to be applicable for cure blowing as well. In melt blowing, the air velocity is maximum at the die face and decreases rapidly with the increasing distance from the die face with a power law dependence.[63,67] The maximum drag force exerted on the fiber jet close to the die face results in maximum fiber drawing and maximum fiber acceleration. As a result, the fiber velocity increases rapidly up to a distance of ∼3−4 cm from the die face, where it attains a maximum value similar in magnitude to the air velocity. Beyond this point, the fiber velocity continues to decay at the same rate as the air velocity.[63−65] Notably, high-speed photography studies of cure blowing (Figure S2) revealed that maximum fiber jet thinning occurs within 0.5 cm of the die face due to the considerably lower viscosity of the monomer mixture feed (∼0.25 Pa s in cure blowing compared to ∼25−150 Pa s for typical polymer feed in melt blowing).[12,69] Consequently, conservation of mass of the liquid filament dictates that a maximum fiber jet velocity will be achieved within 0.5 cm of the die face, which suggests that the difference between the fiber velocity and air velocity profiles in cure blowing would reduce to zero much closer to the die face compared to melt blowing.

While the air velocity profile can be represented by a power law model, mass and momentum balance equations applied to a fiber jet in melt blowing reveal a complex dependence of the fiber velocity on parameters such as the air velocity, fiber jet diameter, and polymer melt viscoelasticity.[68,70] As a result, it is challenging to assess the roles of each relevant parameter and analytically describe the fiber velocity profile. To the best of our knowledge, no analytical models have been reported that can appropriately summarize the fiber velocity. Therefore, we utilized the air velocity profile as a limiting case to approximate the cure blown fiber velocity. The previous discussion on the enhanced fiber acceleration in cure bowing suggests that this

https://doi.org/10.1021/acsapm.3c01083
ACS Appl. Polym. Mater. 2023, 5, 7841−7853

approximation can provide reasonably accurate estimates of the fiber flight times. The power law model developed by Moore et al. to describe the air velocity profile observed in melt blowing using a die geometry very similar to that used in this study is defined as.[63]

$$\frac{v(z)}{v_0} = 1.864\left(\frac{z}{h}\right)^{-0.6321} \quad (5)$$

where $v(z)$ isthe mean air velocity at a distance of z cm from the die face along the fiber spinning axis, v_0 is the mean air velocity at the die face, and h is the sum of the orifice diameter and total air knife gap, where $h \approx 0.5$ cm for the cure blowing die design used in this study. Air flow rates = 0.5−1.5 SCFM used in cure blowing studies correspond to v_0 = 32−109 m/s. The flight times to the light spot and UV exposure times were estimated by integrating eq 5 using proper integration limits where the edge of the light spot is located 4 cm from the die face and the total length of the light spot along the fiber spinning axis is 12 cm. Table 4 lists the estimated values of the flight times to the light spot and UV exposure times for the air flow rates used in this cure blowing study.

Table 4. Fiber Flight Time to the Light Spot and UV Exposure Times for Typical Cure Blowing Air Flow Rates

air flow rate (SCFM)	flight time to light spot (ms)	UV exposure time (ms)
0.5	1.4	13.1
0.75	0.9	8.6
1	0.7	6.2
1.25	0.5	4.8
1.5	0.4	3.9

Morphology Maps: Interdependence of the Characteristic Timescales. The previous sections quantified the competing timescales corresponding to the photopolymerization kinetics, monomer mixture fluid properties, and process operating conditions that dictate the ultimate outcomes of the cure blowing process. Thus, the origins of the fiber morphology transitions may be explained by comparing the relative magnitudes of these characteristic timescales. For instance, the transition from non-fused to fused fiber morphology arises from the balance between vitrification time and UV exposure time, since a smaller UV exposure time compared to t_{vit} implies insufficient curing of the liquid fiber jets that render them susceptible to developing fused junctions after deposition on the collector. Similarly, the propensity to develop non-uniform surface undulations stems from the balance between the fluid relaxation time and flight time to the light spot, since fluid instability-driven surface undulations evolve during liquid fiber jet flight prior to photopolymerization. Thus, a longer fluid relaxation time compared to flight time to the light spot suppresses the growth of surface undulations in the liquid filaments and prevents formation of nonunform fiber diameters.

Two-dimensional morphology maps can thus be phenomenologically constructed in terms of a "kinetic ratio" of UV exposure time and t_{vit} that delineates the non-fused to fused morphology transition, and a "fluid stability ratio" of fluid relaxation time to flight time to the light spot that specifies the transition from uniform to non-uniform fiber diameters. Multiple cure blowing experiments were performed for both thiol-acrylate and thiol-ene model systems by varying the air flow rate, monomer delivery rate, and PEO content in the monomer mixtures. The resulting fiber morphologies were imaged with a VLM and categorized into uniform non-fused, uniform fused, and non-uniform fused fiber morphologies. Figure 9 shows the morphology maps for both model systems obtained at a monomer delivery rate of 0.25 mL/min. Note that the shaded regions are intended as an approximate guide to the eye only. The nonlinear nature of the domain boundaries of the morphology maps further corroborates the complex interplay of different timescales associated with cure blowing in specifying the final fiber morphology. Comparison of the morphology maps constructed for both thiol-acrylate and thiol-ene model systems shows similar trends in fiber morphology evolution with the kinetic and fluid stability ratios, as well as similar magnitudes of the timescale ratios corresponding to the domain boundaries. This indicates that these characteristic timescale ratios that describe the physics and photochemistry of cure blowing successfully capture variations in fiber morphology irrespective of the photopolymerization mechanism. The lack of dependence on the polymerization mechanism further validates the role of vitrification as the primary cause for the photopolymerization kinetics-driven morphology transition.

These morphology maps may also serve as a predictive guide for implementation of new monomer chemistries in cure blowing to obtain fibers with targeted morphologies. As shown in Figure S3, a specific region within the morphology map can

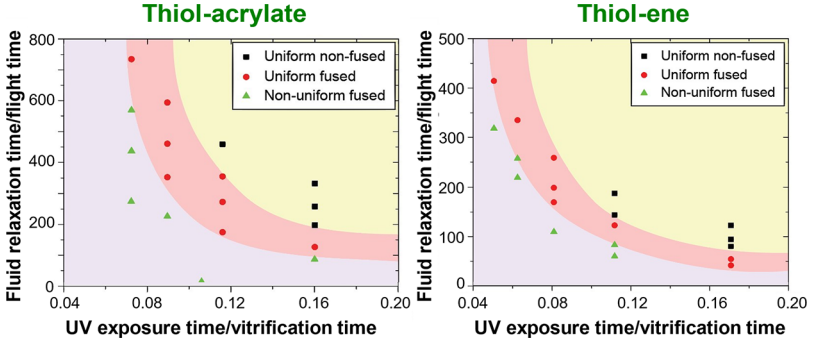

Figure 9. Representative morphology maps for (left) thiol-acrylate and (right) thiol-ene model systems obtained by correlating the cure blown fiber morphology with the ratio of UV exposure time and vitrification time and the ratio of fluid relaxation time and flight time to the light spot. All the data included in the morphology maps were obtained at a monomer delivery rate of 0.25 mL/min where the effective light intensities in the same plane as the fiber path were maintained at 1.5 and 1 W/cm^2 for the thiol-acrylate and thiol-ene model systems, respectively.

https://doi.org/10.1021/acsapm.3c01083
ACS Appl. Polym. Mater. 2023, 5, 7841−7853

be completely defined in terms of the four characteristic timescales. Consequently, the relevant kinetic, material, and process operating parameters can be tuned a priori to fiber spinning to obtain the timescale values needed to obtain the desired fiber morphologies. The ability to predictively determine the necessary cure blowing parameters eliminates the tiral-and-error determination of the appropriate process conditions, enabling rapid real-world optimization of this high-throughput nonwoven fabrication method.

CONCLUSIONS

A semiquantitative framework was developed to correlate the interplay between different categories of parameters with cure blown fiber morphologies, irrespective of the detailed monomer chemistries and underlying mechanisms of cross-linked network formation. This was accomplished by summarizing the contribution of each of these categories in terms of characteristic physical timescales, namely, the vitrification time to describe the photopolymerization kinetics, the fluid relaxation time representing the monomer mixture viscoelastic properties, and the flight times (i.e., UV exposure time and flight time to the light spot) to account for the process operating conditions. Our studies suggest that the vitrification time, rather than the gelation time, best embodies the photopolymerization timescale governing the transition from non-fused to fused fiber morphologies. Two-dimensional morphology maps were constructed to associate cure blown fiber morphologies with the estimated characteristic timescales using a "kinetic ratio" of the UV exposure time and vitrification time and a "fluid stability ratio" of the fluid relaxation time and flight time to the light spot. Similarities in the morphology maps obtained for thiol-acrylate and thiol-ene model systems validate the choice of characteristic timescales to hold true irrespective of the photopolymerization mechanism involved in cure blown network formation. Furthermore, the morphology maps provide a predictive framework that will enable rapid identification and implementation of new monomer chemistries to the cure blowing process. Thus, this study lays the foundation for the development of cure blowing as an industrially relevant fiber manufacturing approach for producing cross-linked synthetic nonwovens with tailored chemical and physical properties for a broad variety applications.

ASSOCIATED CONTENT

Supporting Information

The Supporting Information is available free of charge at https://pubs.acs.org/doi/10.1021/acsapm.3c01083.

Additional figures and experimental results including DMA, high-speed photography, and representative regions of morphology maps and a detailed description and discussion of the TR-FTIR characterization method (PDF)

AUTHOR INFORMATION

Corresponding Author

Christopher J. Ellison − *Department of Chemical Engineering and Materials Science, University of Minnesota, Minneapolis, Minnesota 55455, United States;* orcid.org/0000-0002-0393-2941; Email: cellison@umn.edu

Authors

Aditya Banerji − *Department of Chemical Engineering and Materials Science, University of Minnesota, Minneapolis, Minnesota 55455, United States;* orcid.org/0000-0003-0654-9195

Mahesh K. Mahanthappa − *Department of Chemical Engineering and Materials Science, University of Minnesota, Minneapolis, Minnesota 55455, United States;* orcid.org/0000-0002-9871-804X

Complete contact information is available at: https://pubs.acs.org/10.1021/acsapm.3c01083

Author Contributions

The manuscript was written through contributions of all authors. All authors have given approval to the final version of the manuscript.

Notes

The authors declare no competing financial interest.

ACKNOWLEDGMENTS

The authors gratefully acknowledge 3M for partial financial support. Part of this work was carried out in the Characterization Facility, University of Minnesota, which receives partial support from the NSF through the MRSEC (Award Number DMR-2011401) and the NNCI (Award Number ECCS-2025124) programs. The authors also thank Dr. Heonjoo Ha for his recommendation of utilizing the DMA technique to measure glass transition temperature evolution during cross-linking to better investigate vitrification.

REFERENCES

(1) Russell, S., *Handbook of Nonwovens*; Taylor & Francis: Cambridge, U.K., 2007, 1−15.

(2) Karim, N.; Afroj, S.; Lloyd, K.; Oaten, L. C.; Andreeva, D. V.; Carr, C.; Farmery, A. D.; Kim, I.-D.; Novoselov, K. S. Sustainable Personal Protective Clothing for Healthcare Applications: A Review. *ACS Nano* **2020**, *14*, 12313−12340.

(3) Ghosh, S., Composite Nonwovens in Medical Applications. In *Composite Non-Woven Materials*, Das, D.; Pourdeyhimi, B., Eds.; Woodhead Publishing: Cambridge, U.K., 2014; 211−224.

(4) Lu, P.; Xia, Y. Novel Nanostructures of Rutile Fabricated by Templating against Yarns of Polystyrene Nanofibrils and Their Catalytic Applications. *ACS Appl. Mater. Interfaces* **2013**, *5*, 6391−6399.

(5) Wang, H.; Zhang, Y.; Gao, H. P.; Jin, X. Y.; Xie, X. H. Composite Melt-blown Nonwoven Fabrics with Large Pore Size as Li-ion Battery Separator. *Int. J. Hydrogen Energy* **2016**, *41*, 324−330.

(6) Zhang, Q.; Welch, J.; Park, H.; Wu, C.-Y.; Sigmund, W.; Marijnissen, J. C. M. Improvement in Nanofiber Filtration by Multiple Thin Layers of Nanofiber Mats. *J. Aerosol Sci.* **2010**, *41*, 230−236.

(7) Yesil, Y.; Bhat, G. S. Porosity and Barrier Properties of Polyethylene Meltblown Nonwovens. *J. Text. Inst.* **2017**, *108*, 1035−1040.

(8) Huang, Z.-M.; Zhang, Y. Z.; Kotaki, M.; Ramakrishna, S. A Review on Polymer Nanofibers by Electrospinning and their Applications in Nanocomposites. *Compos. Sci. Technol.* **2003**, *63*, 2223−2253.

(9) Kennedy, K. M.; Bhaw-Luximon, A.; Jhurry, D. Cell-matrix Mechanical Interaction in Electrospun Polymeric Scaffolds for Tissue Engineering: Implications for Scaffold Design and Performance. *Acta Biomater.* **2017**, *50*, 41−55.

(10) Pham, Q. P.; Sharma, U.; Mikos, A. G. Electrospinning of Polymeric Nanofibers for Tissue Engineering Applications: A review. *Tissue Eng.* **2006**, *12*, 1197−1211.

(11) Wente, V. A. Superfine Thermoplastic Fibers. *Ind. Eng. Chem.* **1956**, *48*, 1342−1346.
(12) Ellison, C. J.; Phatak, A.; Giles, D. W.; Macosko, C. W.; Bates, F. S. Melt Blown Nanofibers: Fiber Diameter Distributions and Onset of Fiber Breakup. *Polymer* **2007**, *48*, 3306−3316.
(13) Greiner, A.; Wendorff, J. H. Electrospinning: A Fascinating Method for the Preparation of Ultrathin Fibers. *Angew. Chem., Int. Ed.* **2007**, *46*, 5670−5703.
(14) Shanmuganathan, K.; Sankhagowit, R. K.; Iyer, P.; Ellison, C. J. Thiol−Ene Chemistry: A Greener Approach to Making Chemically and Thermally Stable Fibers. *Chem. Mater.* **2011**, *23*, 4726−4732.
(15) Janes, D. W.; Shanmuganathan, K.; Chou, D. Y.; Ellison, C. J. Soybean Oil Based Fibers Made Without Solvent or Heat. *ACS Macro Lett.* **2012**, *1*, 1138−1142.
(16) Kim, S.-S.; Ha, H.; Ellison, C. J. Soybean Oil-Based Thermoset Films and Fibers with High Biobased Carbon Content via Thiol−Ene Photopolymerization. *ACS Sustainable Chem. Eng.* **2018**, *6*, 8364−8373.
(17) Kim, S.-S.; Lau, C. M.; Lillie, L. M.; Tolman, W. B.; Reineke, T. M.; Ellison, C. J. Degradable Thermoset Fibers from Carbohydrate-Derived Diols via Thiol−Ene Photopolymerization. *ACS Appl. Polym. Mater.* **2019**, *1*, 2933−2942.
(18) Shanmuganathan, K.; Elliot, S. M.; Lane, A. P.; Ellison, C. J. Highly Stretchable Thermoset Fibers and Nonwovens Using Thiol−ene Photopolymerization. *ACS Appl. Mater. Interfaces* **2014**, *6*, 14259−14265.
(19) Fang, Y.; Dulaney, A. D.; Gadley, J.; Maia, J. M.; Ellison, C. J. Manipulating Characteristic Timescales and Fiber Morphology in Simultaneous Centrifugal Spinning and Photopolymerization. *Polymer* **2015**, *73*, 42−51.
(20) Fang, Y.; Dulaney, A. R.; Gadley, J.; Maia, J.; Ellison, C. J. A Comparative Parameter Study: Controlling Fiber Diameter and Diameter Distribution in Centrifugal Spinning of Photocurable Monomers. *Polymer* **2016**, *88*, 102−111.
(21) Fang, Y.; Ha, H.; Shanmuganathan, K.; Ellison, C. J. Polyhedral Oligomeric Silsesquioxane-Containing Thiol−ene Fibers with Tunable Thermal and Mechanical Properties. *ACS Appl. Mater. Interfaces* **2016**, *8*, 11050−11059.
(22) Banerji, A.; Jin, K.; Liu, K.; Mahanthappa, M. K.; Ellison, C. J. Cross-Linked Nonwoven Fibers by Room-Temperature Cure Blowing and in Situ Photopolymerization. *Macromolecules* **2019**, *52*, 6662−6672.
(23) Cramer, N. B.; Bowman, C. N. Kinetics of Thiol−ene and Thiol−acrylate Photopolymerizations with Real-time Fourier Transform Infrared. *J. Polym. Sci., Part A: Polym. Chem.* **2001**, *39*, 3311−3319.
(24) Lee, T. Y.; Smith, Z.; Reddy, S. K.; Cramer, N. B.; Bowman, C. N. Thiol−Allyl Ether−Methacrylate Ternary Systems, Polymerization Mechanism. *Macromolecules* **2007**, *40*, 1466−1472.
(25) Reddy, S. K.; Cramer, N. B.; Bowman, C. N. Thiol−Vinyl Mechanisms. 2. Kinetic Modeling of Ternary Thiol−Vinyl Photopolymerizations. *Macromolecules* **2006**, *39*, 3681−3687.
(26) Cramer, N. B.; Davies, T.; O'Brien, A. K.; Bowman, C. N. Mechanism and Modeling of a Thiol−Ene Photopolymerization. *Macromolecules* **2003**, *36*, 4631−4636.
(27) Carioscia, J. A.; Schneidewind, L.; O'Brien, C.; Ely, R.; Feeser, C.; Cramer, N.; Bowman, C. N. Thiol−norbornene Materials: Approaches to Develop High T_g Thiol−ene Polymers. *J. Polym. Sci., Part A: Polym. Chem.* **2007**, *45*, 5686−5696.
(28) Anseth, K. S.; Wang, C. M.; Bowman, C. N. Reaction Behaviour and Kinetic Constants for Photopolymerizations of Multi(meth)acrylate Monomers. *Polymer* **1994**, *35*, 3243−3250.
(29) Abu-elenain, D. A.; Lewis, S. H.; Stansbury, J. W. Property Evolution during Vitrification of Dimethacrylate Photopolymer Networks. *Dent. Mater.* **2013**, *29*, 1173−1181.
(30) Anseth, K. S.; Bowman, C. N.; Peppas, N. A. Polymerization Kinetics and Volume Relaxation Behavior of Photopolymerized Multifunctional Monomers Producing Highly Crosslinked Networks. *J. Polym. Sci., Part A: Polym. Chem.* **1994**, *32*, 139−147.
(31) Anna, S. L.; McKinley, G. H. Elasto-capillary Thinning and Breakup of Model Elastic Liquids. *J. Rheol.* **2001**, *45*, 115−138.
(32) Yu, J. H.; Fridrikh, S. V.; Rutledge, G. C. The Role of Elasticity in the Formation of Electrospun Fibers. *Polymer* **2006**, *47*, 4789−4797.
(33) Carioscia, J. A.; Lu, H.; Stanbury, J. W.; Bowman, C. N. Thiol-ene Oligomers as Dental Restorative Materials. *Dent. Mater.* **2005**, *21*, 1137−1143.
(34) Lowe, A. B.; Hoyle, C. E.; Bowman, C. N. Thiol-yne Click Chemistry: A Powerful and Versatile Methodology for Materials Synthesis. *J. Mater. Chem.* **2010**, *20*, 4745−4750.
(35) Reddy, S. K.; Okay, O.; Bowman, C. N. Network Development in Mixed Step-Chain Growth Thiol−Vinyl Photopolymerizations. *Macromolecules* **2006**, *39*, 8832−8843.
(36) Anseth, K. S.; Decker, C.; Bowman, C. N. Real-Time Infrared Characterization of Reaction Diffusion during Multifunctional Monomer Polymerizations. *Macromolecules* **1995**, *28*, 4040−4043.
(37) Chiu, Y. Y.; Lee, L. J. Microgel Formation in the Free Radical Crosslinking Polymerization of Ethylene Glycol Dimethacrylate (EGDMA). I. Experimental. *J. Polym. Sci., Part A: Polym. Chem.* **1995**, *33*, 257−267.
(38) Cramer, N. B.; Scott, J. P.; Bowman, C. N. Photopolymerizations of Thiol−Ene Polymers without Photoinitiators. *Macromolecules* **2002**, *35*, 5361−5365.
(39) Reddy, S. K.; Cramer, N. B.; O'Brien, A. K.; Cross, T.; Raj, R.; Bowman, C. N. Rate Mechanisms of a Novel Thiol-ene Photopolymerization Reaction. *Macromol. Symp.* **2004**, *206*, 361−374.
(40) Wen, M.; Scriven, L. E.; McCormick, A. V. Differential Scanning Calorimetry and Cantilever Deflection Studies of Polymerization Kinetics and Stress in Ultraviolet Curing of Multifunctional (Meth)acrylate Coatings. *Macromolecules* **2002**, *35*, 112−120.
(41) Scott, T. F.; Cook, W. D.; Forsythe, J. S.; Bowman, C. N.; Berchtold, K. A. FTIR and ESR Spectroscopic Studies of the Photopolymerization of Vinyl Ester Resins. *Macromolecules* **2003**, *36*, 6066−6074.
(42) Berchtold, K. A.; Randolph, T. W.; Bowman, C. N. Propagation and Termination Kinetics of Cross-Linking Photopolymerizations Studied Using Electron Paramagnetic Resonance Spectroscopy in Conjunction with Near IR Spectroscopy. *Macromolecules* **2005**, *38*, 6954−6964.
(43) Schmidt, L. E.; Leterrier, Y.; Schmäh, D.; Månson, J.-A. E.; James, D.; Gustavsson, E.; Svensson, L. S. Conversion Analysis of Acrylated Hyperbranched Polymers UV-cured Below their Ultimate Glass Transition Temperature. *J. Appl. Polym. Sci.* **2007**, *104*, 2366−2376.
(44) Pfeifer, C. S.; Wilson, N. D.; Shelton, Z. R.; Stansbury, J. W. Delayed Gelation through Chain-transfer Reactions: Mechanism for Stress Reduction in Methacrylate Networks. *Polymer* **2011**, *52*, 3295−3303.
(45) Zhang, Y.; Kranbuehl, D. E.; Sautereau, H.; Seytre, G.; Dupuy, J. Study of UV Cure Kinetics Resulting from a Changing Concentration of Mobile and Trapped Radicals. *Macromolecules* **2008**, *41*, 708−715.
(46) Ye, S.; Cramer, N. B.; Bowman, C. N. Relationship between Glass Transition Temperature and Polymerization Temperature for Cross-Linked Photopolymers. *Macromolecules* **2011**, *44*, 490−494.
(47) Cook, W. D.; Simon, G. P.; Burchill, P. J.; Lau, M.; Fitch, T. J. Curing Kinetics and Thermal Properties of Vinyl Ester Resins. *J. Appl. Polym. Sci.* **1997**, *64*, 769−781.
(48) Kloosterboer, J. G.; Lijten, G. F. C. M. Photopolymers Exhibiting a Large Difference Between Glass Transition and Curing Temperatures. *Polymer* **1990**, *31*, 95−101.
(49) Enns, J. B.; Gillham, J. K. Time−temperature−transformation (TTT) Cure Diagram: Modeling the Cure Behavior of Thermosets. *J. Appl. Polym. Sci.* **1983**, *28*, 2567−2591.
(50) Venditti, R. A.; Gillham, J. K. A Relationship Between the Glass Transition Temperature (T_g) and Fractional Conversion for Thermosetting Systems. *J. Appl. Polym. Sci.* **1997**, *64*, 3−14.

https://doi.org/10.1021/acsapm.3c01083
ACS Appl. Polym. Mater. 2023, 5, 7841−7853

(51) Corezzi, S.; Fioretto, D.; Puglia, D.; Kenny, J. M. Light Scattering Study of Vitrification during the Polymerization of Model Epoxy Resins. *Macromolecules* **2003**, *36*, 5271−5278.
(52) Belmonte, A.; Däbritz, F.; Ramis, X.; Serra, A.; Voit, B.; Fernández-Francos, X. Cure Kinetics Modeling and Thermomechanical Properties of Cycloaliphatic Epoxy-anhydride Thermosets Modified with Hyperstar Polymers. *J. Polym. Sci., Part B: Polym. Phys.* **2014**, *52*, 1227−1242.
(53) Boger, D. V.; Yeow, Y. L. The Impact of Ideal Elastic Liquids in the Development of Non-Newtonian Fluid Mechanics. *Exp. Therm. Fluid Sci.* **1992**, *5*, 633−640.
(54) Dontula, P.; Macosko, C. W.; Scriven, L. E. Model Elastic Liquids with Water-soluble Polymers. *AIChE J.* **1998**, *44*, 1247−1255.
(55) Tirtaatmadja, V.; McKinley, G. H.; Cooper-White, J. J. Drop Formation and Breakup of Low Viscosity Elastic Fluids: Effects of Molecular Weight and Concentration. *Phys. Fluids* **2006**, *18*, No. 043101.
(56) Bhat, P. P.; Appathurai, S.; Harris, M. T.; Pasquali, M.; McKinley, G. H.; Basaran, O. A. Formation of Beads-on-a-string Structures during Break-up of Viscoelastic Filaments. *Nat. Phys.* **2010**, *6*, 625−631.
(57) Goldin, M.; Yerushalmi, J.; Pfeffer, R.; Shinnar, R. Breakup of a Laminar Capillary Jet of a Viscoelastic Fluid. *J. Fluid Mech.* **1969**, *38*, 689−711.
(58) Oliveira, M. S.; Yeh, R.; McKinley, G. H. Iterated Stretching, Extensional Rheology and Formation of Beads-on-a-string Structures in Polymer Solutions. *J. Non-Newton. Fluid Mech.* **2006**, *137*, 137−148.
(59) Regev, O.; Vandebril, S.; Zussman, E.; Clasen, C. The Role of Interfacial Viscoelasticity in the Stabilization of an Electrospun Jet. *Polymer* **2010**, *51*, 2611−2620.
(60) Stelter, M.; Brenn, G.; Yarin, A. L.; Singh, R. P.; Durst, F. Investigation of the Elongational Behavior of Polymer Solutions by Means of an Elongational Rheometer. *J. Rheol.* **2002**, *46*, 507−527.
(61) Campo-Deaño, L.; Clasen, C. The Slow Retraction Method (SRM) for the Determination of Ultra-short Relaxation Times in Capillary Breakup Extensional Rheometry Experiments. *J. Non-Newton. Fluid Mech.* **2010**, *165*, 1688−1699.
(62) McKinley, G. H.; Tripathi, A. How to Extract the Newtonian Viscosity from Capillary Breakup Measurements in a Filament Rheometer. *J. Rheol.* **2000**, *44*, 653−670.
(63) Moore, E. M.; Papavassiliou, D. V.; Shambaugh, R. L. Air Velocity, Air Temperature, Fiber Vibration and Fiber Diameter Measurements on a Practical Melt Blowing Die. *Int. Nonwovens J.* **2004**, *13*, 1558925004os−155892500413os.
(64) Wu, T. T.; Shambaugh, R. L. Characterization of the Melt Blowing Process with Laser Doppler Velocimetry. *Ind. Eng. Chem. Res.* **1992**, *31*, 379−389.
(65) Xie, S.; Han, W.; Jiang, G.; Chen, C. Turbulent Air Flow Field in Slot-die Melt Blowing for Manufacturing Microfibrous Nonwoven Materials. *J. Mater. Sci.* **2018**, *53*, 6991−7003.
(66) Xie, S.; Zeng, Y. Online Measurement of Fiber Whipping in the Melt-Blowing Process. *Ind. Eng. Chem. Res.* **2013**, *52*, 2116−2122.
(67) Bresee, R. R.; Ko, W.-C. Fiber Formation During Melt Blowing. *Int. Nonwovens J.* **2003**, *12*, 21−28.
(68) Shambaugh, B. R.; Papavassiliou, D. V.; Shambaugh, R. L. Next-Generation Modeling of Melt Blowing. *Ind. Eng. Chem. Res.* **2011**, *50*, 12233−12245.
(69) Tan, D. H.; Zhou, C.; Ellison, C. J.; Kumar, S.; Macosko, C. W.; Bates, F. S. Meltblown fibers: Influence of viscosity and elasticity on diameter distribution. *J. Non-Newton. Fluid Mech.* **2010**, *165*, 892−900.
(70) Uyttendaele, M. A. J.; Shambaugh, R. L. Melt Blowing: General Equation Development and Experimental Verification. *AIChE J.* **1990**, *36*, 175−186.

https://doi.org/10.1021/acsapm.3c01083
ACS Appl. Polym. Mater. 2023, 5, 7841−7853